Origin of High Optical Contrast in Zinc-Zinc Oxide Electrodeposits for Dynamic Windows

Cheon Woo Moon[a], Nikhil C. Bhoumik[a], Profulla Mondol[a], Sung Hyuk Park[b], Ho Won Jang[b], and Christopher J. Barile[a,*]

[a] Department of Chemistry, University of Nevada, Reno, Reno, NV 89557, USA
[b] Department of Materials Science and Engineering, Seoul National University, Seoul 08826, Republic of Korea

[*]E-mail: cbarile@unr.edu

Abstract

The control of solar light and heat emission through windows is an important strategy for increasing the energy efficiency of buildings. Reversible Zn electrodeposition has recently emerged as a promising method for constructing electronically tintable robust dynamic windows. In Zn electrodeposits formed from dimethyl sulfoxide (DMSO) electrolytes during device tinting, we observe extraordinary absorption that is in excess of what is predicted by the Beer-Lambert law for a uniform Zn thin film. The charge required to electroplate these films is abnormally low, significantly less than previously reported dynamic windows based on reversible metal electrodeposition, which facilitates the construction of large-area devices that switch uniformly. Finite-difference time-domain (FDTD) simulations are used to investigate the origin of this enhanced absorption, which arises from plasmonic effects among the Zn nanostructures and ZnO dendrites in the film. The dielectric ZnO dendrites promote absorption via slit-like Zn-dielectric-Zn structures that from hybrid surface plasmon resonance at metal walls. Through these investigations, we provide design principles to construct low-charge and high-contrast metal and metal oxide-based dynamic windows.

Keywords:

Dynamic windows, Zn, electrodeposition, plasmon resonance, finite-difference time-domain (FDTD)

1. Introduction

Increasing building energy efficiency is a crucial component of mitigating climate change due to the large quantity of energy consumed in buildings.[1-4] For this application, two types of technologies, dynamic windows that modulate light coming from the sun, and radiative cooling[5-7], which focuses on the energy going out from the Earth, have emerged. Dynamic windows, which possess electronically switchable transmission, have received great attention due to their ability to increase building energy efficiency via lighting, heating, and cooling savings.[8-10] Additionally, dynamic windows are more aesthetically pleasing than blinds because they maintain the window view. Performance attributes including durability, bistability, switching speed, cost, power requirements, and optical contrast must be considered and improved when developing practical dynamic windows.[11, 12] Polymer-dispersed liquid crystals and electrochromic materials such as polymers and small molecules have been extensively studied as potential approaches for constructing dynamic windows, but these technologies have not yet been widely commercialized due to a variety of problems.[12, 13] Recently, reversible metal electrodeposition has emerged as a promising alternative to developing dynamic windows.

Reversible metal electrodeposition is a promising alternative to competing dynamic window technologies such as liquid crystals and electrochromic materials.[13, 14] Metals generally have a larger imaginary part of their refractive index (k) across the infrared, visible, and ultraviolet portions of the electromagnetic spectrum, which is related to their absorption coefficient, than electrochromic polymers and metal oxides. A thin film of metal can effectively block light even at thicknesses of 20-30 nm.[15-17] By comparison, electrochromic oxide and polymer materials typically require micron-thick films to reach opacity.[18-20] Moreover, vivid

RGB colors can be obtained if combined with photonic-plasmonic platforms.[21, 22] Furthermore, because reversible metal electrodeposition devices can be constructed through solution processable methods, they do not require expensive vacuum-based facilities such as the sputtering chambers typically used to deposit inorganic electrochromic materials.

To analyze the optical properties of dynamic windows based on reversible metal electrodeposition, the Beer-Lambert law has been used, which assumes there is an exponential relationship between the thickness of the film and transmission. However, this assumption could lead to an erroneous estimation of the optical properties of the dynamic window as there are multiple light interactions possible within the inside film volume.[23] For example, Cu-Pb electrodeposits have previously been demonstrated to grow as pillars, which results in less efficient light blocking compared to an ideal thin film.[24] In this manuscript, we found that Zn electrodeposits block light more efficiently than the theoretical value of a perfectly uniform thin film of equivalent charge density because of plasmon resonance within the electrodeposits that results in enhanced absorption. We thoroughly investigate the origin of this enhanced absorption as it relates to plasmonic effects within the nanostructured Zn and ZnO in the films.

A collective oscillation between electrons in metals and photons is called plasmon resonance. When the collective oscillation happens at metal-dielectric interfaces, propagating electromagnetic waves form at the interface which are called surface plasmon polaritons. When the size of the metal electrodeposits is much smaller than the wavelength of the incident light, then the plasmons are confined in a small volume, resulting in localized surface plasmon resonance, which exhibits unique optical properties. Additionally, structural factors such as size, shape, and periodicity contribute to the optical properties of the plasmonic nanostructure. Although most research on plasmonic materials focuses on Au and Ag due to their high

plasmonic quality factors in the visible spectrum,[25] we investigate Zn-based plasmonic systems and also discuss other non-noble metal-based plasmonic systems including Cu, Bi, and Ni in the context of dynamic windows.[26]

The role Zn nanostructures play in efficiently blocking light in dynamic window electrodeposits is, as of yet, unclear. To obtain a high-contrast and efficient dynamic window, an understanding of the coloration principle is necessary. To quantify how efficient tinting occurs in dynamic windows, charge density (or its inverse, which is termed coloration efficiency) is an important metric. A lower charge density indicates that less energy per unit area is required for electrodeposition, which results in energy-efficient coloration. Furthermore, devices with lower charge density require less current to switch at a given speed to a given transmission level. Because reduced switching currents result in a smaller voltage drop across the transparent conducting working electrode of the device, larger dynamic windows using reversible metal electrodeposition can be constructed that maintain uniform switching based on diffusion-limited metal electrodeposition.[27] For this reason, decreasing charge density is a crucial strategy in the construction of large-area metal-based dynamic windows that switch uniformly. For example, with polymer, the charge density required to reach 10% transmission is 2-3 times less than previous reversible metal electrodeposition devices.[16]

In this manuscript, to understand the optical properties of Zn electrodeposits as related to dynamic windows, we investigated the light-blocking properties of Zn electrodeposits from Zn DMSO electrolytes under different conditions. Our spectroelectrochemical results demonstrate that due to their unique nanostructures, the transmission of the electrodeposits can be lower than what is predicted for a perfectly uniform thin Zn film produced from an equivalent quantity of charge during electrodeposition. In-depth modeling of the various Zn and ZnO nanostructures

using finite-difference time-domain (FDTD) simulations show that absorption is enhanced due to hybrid plasmon resonance in slit-like structures caused by ZnO dendrites embedded in Zn. Collective plasmon resonance also contributes to the optical properties of the films and is caused by the compact alignment of small Zn nanoparticles. These nanostructured morphologies were also applied to other electrochemically-active metals relevant to metal-based dynamic windows, which could inspire future electrode design principles to create high-contrast and large-area dynamic windows.

2. Results and Discussion

2.1 Zn Nanoparticle Electrodeposits

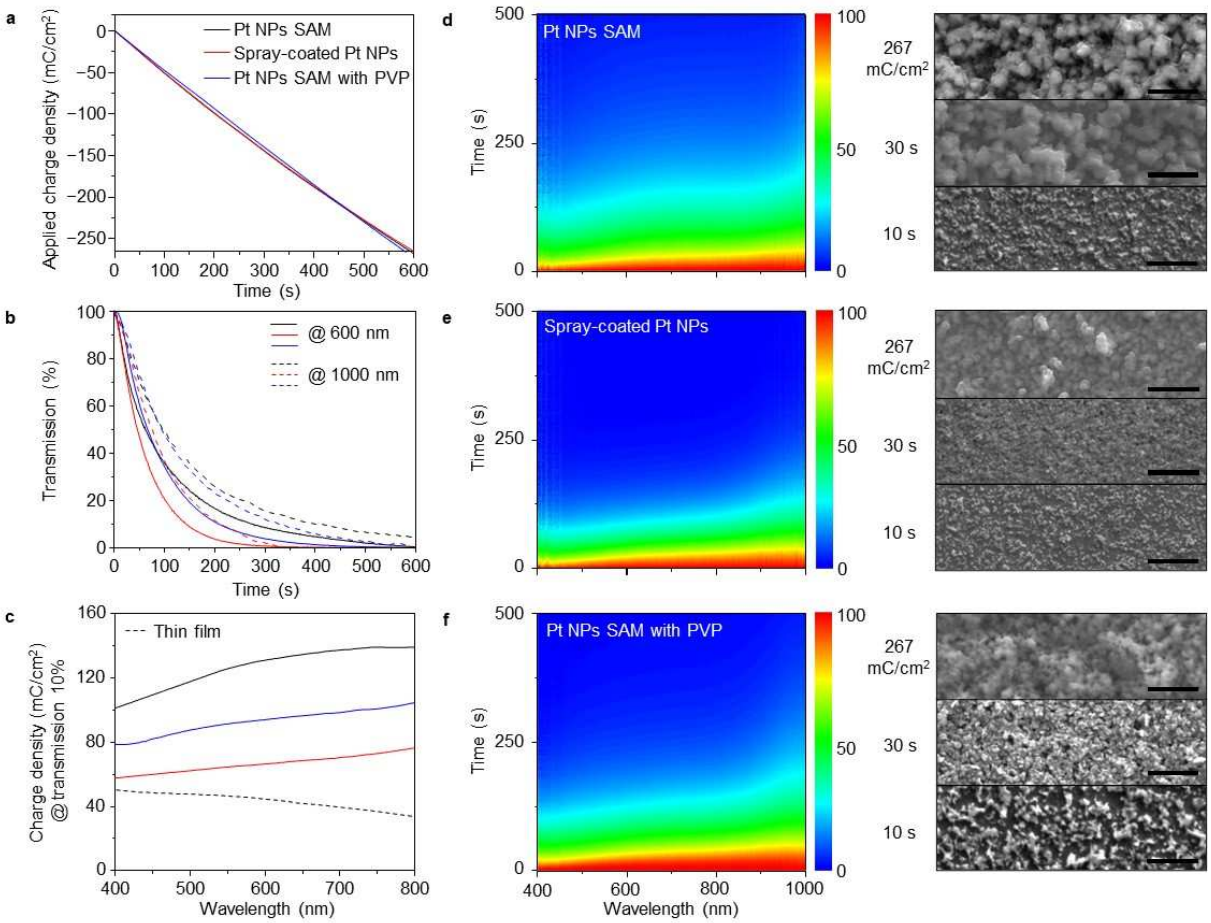

Fig. 1 Spectroelectrochemical properties of Zn electrodeposits from DMSO electrolyte (low concentration). −0.9 V vs. Zn/Zn^{2+} was applied with a three-electrode configuration in a DMSO

electrolyte containing 50 mM $Zn(CH_3COO)_2$, 50 mM $ZnBr_2$, and 67 mM $NaCH_3COO$). Zn electrodeposits over ITO glass with self-assembled Pt NPs (black line), spray-coated Pt NPs (red line), and with addition of PVP to the electrolyte over ITO glass with self-assembled Pt NPs (blue line). (a) Chronocoulometry profiles. (b) Transmission at 600 (solid line) and 1,000 (dotted line) nm as a function of time. (c) Charge density at 10% transmission accompanied with simulated uniform Zn thin film/ITO- glass (black dotted line, (--)). Transmission (%) as a function of wavelength and time for (d) Pt NPs SAM, (e) Spray-coated Pt NPs, and (f) Pt NPs SAM with PVP. Right side: corresponding scanning electron microscope (SEM) images are annotated according to the time and charge density (10 s after applying potential, 30 s after applying potential, and after application of 267 mC/cm^2). Scale bars equal to 1 μm in all SEM images.

To experimentally investigate the optical properties of Zn nanoparticle electrodeposits, low-concentration DMSO electrolytes (50 mM $Zn(CH_3COO)_2$, 50 mM $ZnBr_2$, 67 mM $NaCH_3COO$) were first adopted, and three different electrodeposition conditions were considered. The first condition is electrodeposition on a tin-doped indium oxide (ITO) glass working electrode modified with a self-assembled monolayer (SAM) of Pt nanoparticles (Pt NPs SAM).[15] The second condition is electrodeposition on a Pt-modified ITO working electrode by spray coating (spray-coated Pt NPs).[28] The last condition is electrodeposition on an ITO glass working electrode modified with a SAM of Pt nanoparticles and polyvinylpyrrolidone (PVP) polymer in electrolyte (Pt NPs SAM with PVP). Polymers have been previously shown in metal electrodeposition systems to improve electrodeposit uniformity through a charge-adsorption mechanism,[16] and PVP is used as the capping ligand on the commercially purchased 3 nm Pt nanoparticles. For these reasons, we were interested in the effect of adding PVP to the electrolyte.

As shown in Fig. 1a, the applied charge density profile over time does not significantly differ between the three cases. The corresponding chronoamperometry profile (Fig. S1a) shows there is a difference in nucleation. Normalized current-time curves indicate mixed instantaneous and progressive nucleation during the initial stage of electrodeposition (Fig. S1b). Looking at the transmission at 600 and 1,000 nm, 10% transmission is achieved first in the spray-coated Pt NPs

and for the Pt NPs SAM (Fig. 1b). All three cases possess higher charge density values in the entire visible light wavelengths than an ideal perfectly uniform thin Zn film of equivalent charge density, as calculated by FDTD modeling (Fig. 1c). For example, the charge density to achieve 10 % transmission at 600 nm with an ideal uniform Zn film is 44 mC/cm^2. Zn electrodeposits with Pt NPs SAM, spray-coated Pt NPs, and Pt NPs SAM with PVP experimentally yielded 131, 66, and 94 mC/cm^2 at 600 nm, respectively. Detailed simulation results with the thin film are displayed in Fig. S2. The uniform Zn thin film with surrounding DMSO electrolyte and ITO (80 nm)/glass is more transparent than the isolated uniform Zn thin film because of interference with the ITO (80 nm)/glass as the thickness of Zn film is thin enough ($\ll \lambda/4n$, where λ is the wavelength of incident light, and n is the real part of the refractive index).[29] Transmission maps across the 400 to 1,000 nm wavelengths during 500 s of electrodeposition are shown in Figs. 1d ~ 1f. Overall, the low-transmission state (transmission <10%) transition is the fastest with the spray-coated Pt NPs. Unlike the thin film simulation, the transmission decreases relatively quickly at shorter wavelengths. The interpretation of this result will be discussed in detail in the next section. For reference, spectroelectrochemical properties of Zn electrodeposits from pristine ITO (without Pt nanoparticles) are also measured. In this case, the transmission declines less rapidly than all other cases above due to the poor, aggregated morphology of the electrodeposits as determined previously for other reversible metal electrodeposition systems (Fig. S3).[24]

As can be seen from the SEM images in the right column (Figs. 1d ~ 1f), the Zn electrodeposits consist of nanoparticles. There are empty spaces between the nanoparticles because the particle density is not enough to fill all directions. The morphologies found in the SEM images are also confirmed using atomic force microscopy (AFM) (Figs. S4 and S5).

Considering the relationship between morphology and transmission, Zn electrodeposits on ITO glass with Pt NPs SAM, which have the largest voids in the Zn electrodeposits, also have the worst light-blocking properties. X-ray diffraction (XRD) of Zn electrodeposits shows that Zn and ZnO both are present in the electrodeposits in all cases (Fig. S6). Cross-sectional SEM imaging of the electrodeposits obtained after applying a charge density of 267 mC/cm^2 indicates that the structure is porous (Fig. S7). While a thickness of ~127 nm is expected from a charge density of 267 mC/cm^2 for a compact Zn film, the measured thickness from the cross-sectional SEM of the Zn electrodeposits on ITO glass with spray-coated Pt NPs, for example, is ~360 nm, which indicates that the electrodeposits are substantially porous.

2.2 Zn Nanoparticle Array Simulations

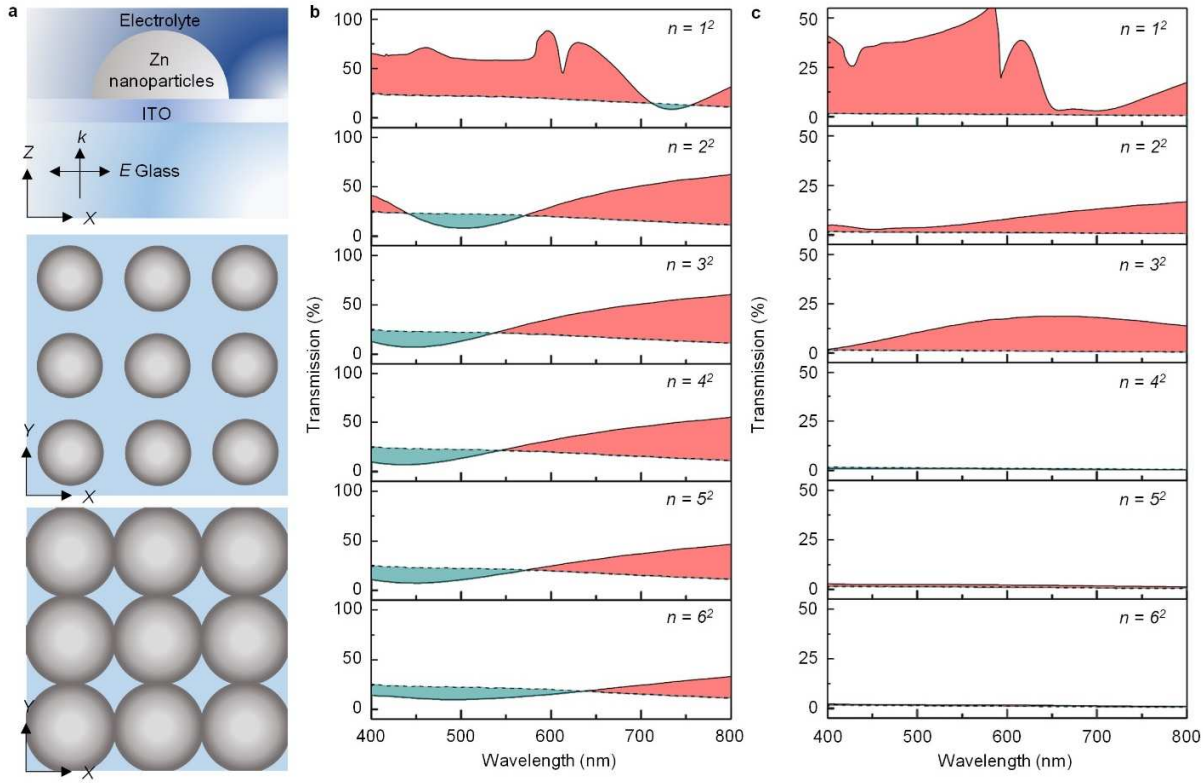

Fig. 2 FDTD simulation of square-arrayed hemisphere particle lattices. The total number of hemispherical nanoparticles is indicated as n. (a) Schematic representation of the configuration (top). P-polarized plain wave is illuminated from the glass side to the electrolyte (outdoor transmission, electric field vector and wavevector are denoted as E and k). Case examples for $n = 3^2$ with gray Zn nanoparticles are represented in the middle and bottom (amount of Zn is equivalent to 15 and 40 nm uniform Zn films). A 400×400 nm^2 unit cell is used. Transmission of Zn nanoparticle film equivalent to charge density of (b) 15 and (c) 40 nm Zn thin film with respect to the wavelength and n. The dotted line (--) indicates the transmission of uniform Zn films with thicknesses of 15 nm (b) and 40 nm (c) on ITO on glass in DMSO electrolyte. Positive/negative transmission (T) gain (= $T_{\text{Nanoparticle array}} - T_{\text{Ideal thin film}}$) is indicated as red/blue compared to uniform thin films.

To begin modeling the experimental optical data, a square-arrayed hemispherical particle lattice was first utilized using p-polarized light incident on the glass side of the device (Fig. 2a, top). Zn nanoparticle films were modeled that would require the same charge density of electrodeposited Zn equivalent to 15 (Fig. 2b) and 40 (Fig. 2c) nm perfectly uniform and compact Zn thin films. This approach enables us to evaluate the effect of increasing the number of particles (n) from 1^2 to 6^2 and also the effect of interparticle contacts. Increasing the number of particles make results in hemispherical particles with smaller diameters because they are constructed with the same total mass. As an example, for the case of $n = 3^2$, when the charge density is equivalent to the 15 nm uniform film, the particles are 50 nm radius hemispheres (Fig 2a, middle), while the 40 nm equivalent case yields 70 nm radius hemispheres (Fig 2a, bottom). The detailed schemas of particle arrangement are depicted in Fig. S8.

Fig. 2b shows the differences in transmission obtained by increasing n compared to the case of a uniform 15 nm Zn thin film with the same amount of charge density required for Zn electrodeposition as the nanoparticle arrays. When n is increased from 1^2 to 6^2, the radius of the hemisphere particle changes from 105 to 32 nm. The transmission gain is positive in the entire visible light region (400 to 700 nm) when $n = 1^2$. In this case, the size of the gap between the nanoparticles is 191 nm, which is close in size to that of each nanoparticle. On the other hand,

when $n = 6^2$, the nanoparticle array exhibits a lower transmission than the equivalent uniform Zn thin film from 400 to 635 nm, which is advantageous for the application of designing dynamic windows with excellent light-blocking capabilities. The interparticle gap for this case is 3.3 nm, which is much smaller than that of the individual particle size (32 nm). It is known that when nanoparticles are located close enough, strong absorption can be induced because of the hybridization of plasmon modes.[30] As a whole, these simulation results indicate that enhanced light blocking occurs in the visible light region when particles are closely packed with some amount of interparticle gaps.

Fig. 2c shows the differences in transmission obtained by increasing n compared to the case of a uniform 40 nm Zn thin film with the same amount of charge density required for Zn electrodeposition as the nanoparticle arrays. When n is changed from 1^2 to 6^2, the radius of the hemisphere particles changes from 145 to 49 nm. Unlike the cases in Fig. 2b, the particles overlap with each other at $n \geq 3^2$. The overlap of the particles is significant at $n \geq 3^2$ and, as a result, the particle arrays gradually converge into uniform thin film as n increases. Therefore, no significant benefit in transmission is observed. When the interparticle gap spacing is larger, plasmon mode hybridizations between the particles are weaker, and therefore the probability of re-interaction of the reflected wave decreases, which leads to increased transmission. The response of each particle will approach that of an isolated particle which corresponds to an ideal Mie solution.[31] If the size of particles becomes larger, the total extinction efficiency and scattering compared to absorption increase.[32, 33] As seen in the $n = 1^2$ cases of Figs. 2b and 2c, distinct optical properties (e.g. an absorption peak located at 612 and 594 nm, respectively) are manifested as a result of emerging far-field coupling.[34]

Reversing the light propagation direction such that it is incident on the electrolyte first does not affect the resulting transmissions (except for $n = 1^2$) compared to light incident on the glass (Fig. S9). Furthermore, reflectance of the Zn nanoparticle arrays is reduced in all cases compared to the uniform Zn thin films because part of the reflected energy from nanoparticles is converted to form surface plasmon resonance (Figs. S10 and S11). Because the sum of absorption, transmission, and reflection is unity, the enhanced absorption of Zn nanoparticles leads to a lowering in transmission. In an attempt to more accurately model the actual Zn electrodeposits, we also investigated the effect of surface oxidation of Zn (Figs. S8c and S12). It was assumed that 20% of the outer radius of the hemisphere was oxidized to ZnO, which corresponds to nearly half (49%) of the volume of the original sphere. Although the light-blocking abilities of the nanoparticle arrays are less than those of the unoxidized arrays presented in Fig. 2b, the transmission values of the core-shell oxidized particles are still less than those at shorter wavelengths of visible light due to enhanced absorbance caused by plasmon resonance even with the highest modeled particle number of $n = 6^2$.

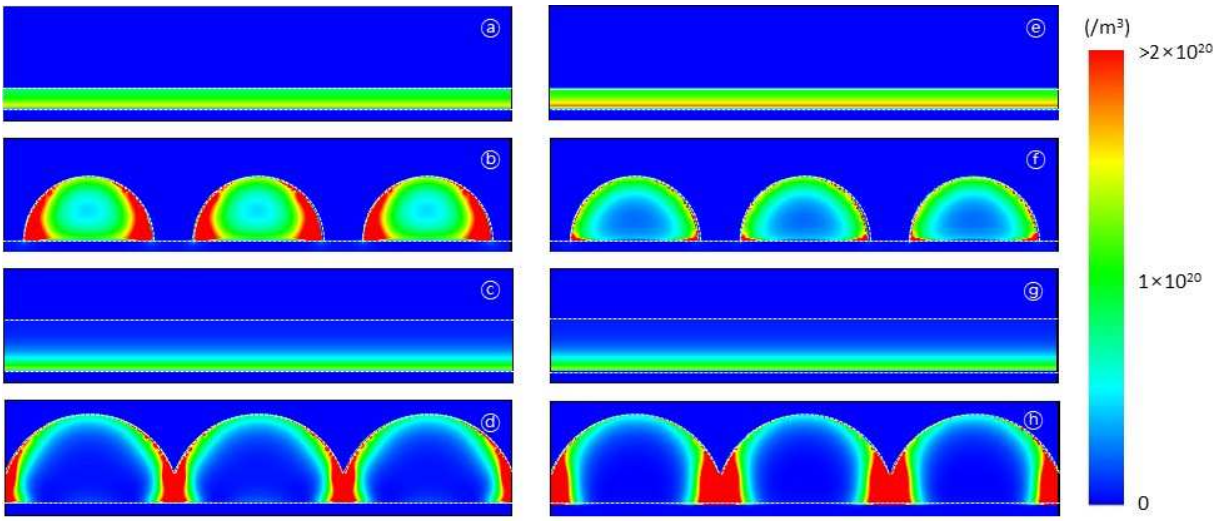

Fig. 3 Volume absorption mapping in 90 × 400 nm^2 cell. ⓐ ~ ⓓ depict absorption mapping in 500 nm wavelength. ⓔ ~ ⓗ depict absorption mapping in 700 nm wavelength. ⓐ and ⓔ depict the uniform 15 nm Zn thin film. ⓑ and ⓕ correspond to the Zn hemisphere square array of $n = 3^2$ structures, and their charge density is equivalent to that of the uniform 15 nm Zn thin film. ⓒ and ⓖ depict the uniform 40 nm Zn thin film. ⓓ and ⓗ correspond to the Zn hemisphere particle square array of $n = 3^2$ structures, and their charge density is equivalent to that of the uniform 40 nm thin film. P-polarized plain wave is illuminated from the ITO side (outdoor transmission), and the electric field vector and wavevector are denoted as E and k, respectively. Absorbed power per unit volume is normalized to the source power.

The absorption profiles of nanostructures discussed in Fig. 2 are visualized to investigate underlying optical phenomena (Fig. 3). 15 (ⓐ and ⓔ) and 40 (ⓒ and ⓖ) nm Zn uniform thin films and hemisphere particle arrays (ⓑ, ⓕ, ⓓ, and ⓗ) corresponding to $n = 3^2$ containing the same charge density as the Zn thin films are displayed. Comparing (ⓐ and ⓔ) and (ⓑ and ⓕ), which have the same charge density, there is a decrease in transmission at 500 nm and an increase in transmission at 700 nm for the nanoparticle arrays compared to the uniform thin film (Fig. 2b). The absorption is facilitated at the interface between the Zn hemispheres and ITO at 500 nm. In other cases, comparing (ⓒ and ⓖ) and (ⓓ and ⓗ), which have the same charge density, there is an increase in transmission at both 500 and 700 nm for the nanoparticle arrays compared to the uniform thin film (Fig. 2c). Absorption primarily happens at a V-shaped groove formed by hemisphere particle overlap, and the interface between Zn hemispheres and ITO does not contribute to the absorption.

More detailed information comes from field profile analysis. As shown in Figs. S13a and S13b, in the uniform thin film, only the electric field component parallel to the incident electric field (E_x) exists because electric field parallel to the interface cannot excite plasmon polariton,

which is prohibited from the boundary conditions.[35] Figs. S13c ~ 13f show the presence of the E_z component in the hemisphere array. This analysis demonstrates the existence of plasmon resonance in the Zn nanoparticle array. If there is an interparticle gap, a relatively strong electric field (E_z) is observed on the ITO side as shown in Figs. S13c and S13d, which indicates that there is a plasmon resonance from the ITO interface. The strong E_x at the interparticle gap is evidence of hybrid plasmon resonance.[36] If there is no interparticle gap, the overall electric field is concentrated in a V-shaped groove region between the spheres as shown in Figs. S13e and S13f. The electric field (E_z) at the interface of the Zn hemisphere particle and ITO is weakened, which results in weak plasmon resonance arising from the Zn hemisphere particle and ITO.

Furthermore, if the simulation is performed using a spherical particle instead of a hemisphere particle, it is difficult for the nanoparticle array to possess a lower transmission than the uniform thin film with the corresponding same amount of charge density (Fig. S14). This difference arises because the hot spot (high electric field intensity region) caused by plasmon resonance only exists on the point-like contact positions on ITO. In the hemisphere case, this hot spot is widely spread in the areal interface between Zn hemisphere particles and ITO, and even inside of the hemispheres as well. In other words, the hemisphere shape possesses widely distributed hot spots with large electric fields.[37, 38] In addition, this hemisphere model resembles actual nanoparticle growth models used for electrodeposits.[39, 40] When the particles overlap, the light-blocking capability of the nanostructure is worsened because it resembles a uniform thin film, and so the benefit from plasmon resonance disappears.

2.3 Porosity Simulation of Zn

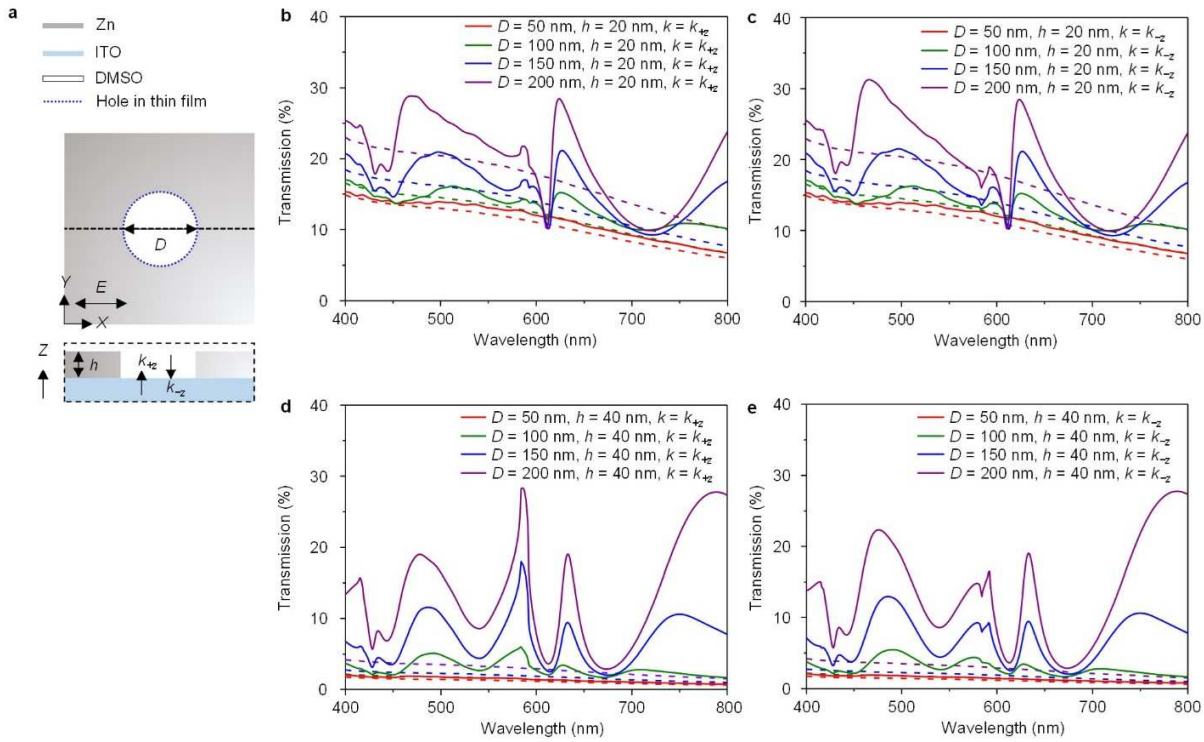

Fig 4. Porosity effect on Zn film. (a) Simulation scheme of uniform Zn thin film containing nanoholes of diameter D in 400 × 400 nm^2 unit cell. The height of the film is indicated as h. The electric field vector and wavevector are denoted as E and k, respectively. Outdoor and indoor illuminations are represented as wavevectors as k_{+z} and k_{-z}, respectively. The dotted line (--) indicates the transmission of uniform Zn thin films without nanoholes containing the same charge density. Nanohole-incorporated 20 nm Zn thin films with (b) outdoor and (c) indoor illumination. Nanohole-incorporated 40 nm Zn thin films with (d) outdoor and (e) indoor illumination.

As discussed in Fig. S7, we gained insight into the optical properties of the Zn electrodeposits by comparing theoretical uniform thin films and the actual Zn electrodeposits, which consist of a porous structure. The aforementioned Zn nanoparticle simulations do not deeply consider electrodeposit porosity. Therefore, model porous structures are constructed without particles. As shown in Fig. 4a, a cylinder-shaped hole was introduced in the Zn film over ITO in the DMSO electrolyte. A cross-sectional view through the dotted line is also depicted below. Simulations are achieved by changing the hole's size, the thin film's thickness, and the light propagation direction. P-polarized light was only considered due to the symmetry of the

cylindrical hole in the *X* and *Y* axes. In all simulation cases from Figs. 4b to Fig. 4d, when the hole size is small (D = 50 nm), the transmission is almost identical to the ideal thin film with the same charge density. In Figs. 4b and 4c, in the case of relatively small thicknesses (h = 20 nm), the transmission is lower than that of the thin film in a limited wavelength region under specific resonance conditions, but it is mostly higher than that of the thin film with the same charge density. When the thickness is larger (h = 40 nm), as shown in Figs. 4d and 4e, the transmission is not lower than that of the equivalent charge density thin film at any wavelength. Porous structures, especially with large-sized pores (> 100 nm), have a noticeable adverse effect on light-blocking properties. The direction of light does not significantly affect transmission if very large-sized pores (> 200 nm) are absent.

As the size of the nanoholes in the thin metal film increases, the volume portion of the metal wall where the generated plasmon can confine increases, which results in reducing the plasmon attenuation. As a result, the surface plasmon propagation length increases, which facilitates light transmission through the nanohole.[41] The absorption and electric field profiles were investigated in the 20 nm Zn film with a 50 nm diameter pore (Fig. S15). Compared to the uniform absorption profile in the 20 nm Zn thin film (Fig. 5c) in the next section, a reduced absorption is observed near the pore edge at the outgoing side of light propagation. The existence of a E_z component indicates that there is plasmon resonance in the structure. Although there is a small enhancement of absorption from plasmon resonance both from the edge sides of the hole, this contribution is relatively small. Taken together, these analyses demonstrate that nanoholes act as transmission increasing sites.

2.4 Zn Electrodeposits with Dendrites

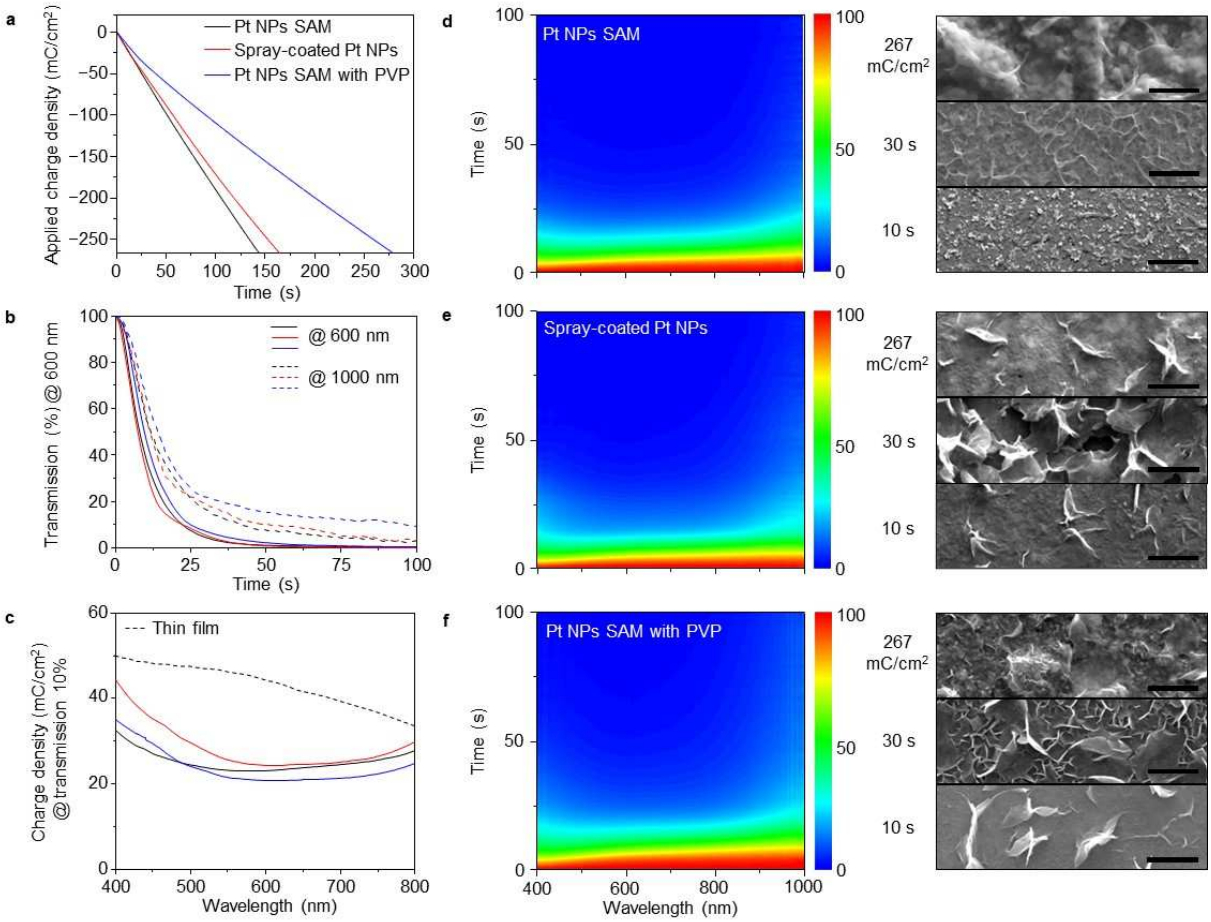

Fig. 5 Spectroelectrochemical properties of Zn electrodeposits from DMSO electrolyte (high concentration). –0.9 V vs. Zn/Zn^{2+} was applied with a three-electrode configuration in DMSO containing 300 mM $Zn(CH_3COO)_2$, 300 mM $ZnBr_2$, and 400 mM $NaCH_3COO$. Zn electrodeposits over ITO glass functionalized with self-assembled Pt NPs (black line). Zn electrodeposits over ITO glass functionalized with spray-coated Pt NPs (red line). Zn electrodeposits with addition of PVP to electrolyte over ITO glass functionalized with self-assembled Pt NPs (blue line). (a) Chronocoulometry profiles. (b) Transient at 600 (solid line) and 1,000 (dotted line) nm as a function of time. (c) Charge density at transmission 10%. Accompanied with ideal simulated Zn thin film/ITO glass (black dotted line, (--)). Transmission (%) as a function of wavelength and time for (d) Pt NPs SAM, (e) Spray-coated Pt NPs, and (f) Pt NPs SAM with PVP. Right side: corresponding scanning electron microscope (SEM) images are annotated according to the time and charge density at 10 s after applying potential, at 30 s after applying potential, and after 267 mC/cm^2 of charge is passed. Scale bars equal to 1 μm in all SEM images.

Instead of the electrodeposits consisting of only nanoparticles, dendrite co-deposition occurs when a high-concentration Zn DMSO electrolyte is used, and so we also investigated the spectroelectrochemical properties of this system (Fig. 5). Aside from the difference in electrolyte

concentration, the three conditions adopted are the same as those used in Fig. 1. As can be seen in Fig. 5a, in the case of Pt NPs SAM with PVP, the charge density consumption rate is significantly less than for the other two cases. Inspection of the chronoamperometric profiles (Fig. S16) reveals that all cases deviate from spherical nucleation profiles. By referring to the corresponding SEM images at 30 s after applying potential in Fig. 5d ~ 5f, the dendrite density is lowest with spray-coated Pt NPs, which has the worst light-blocking behavior among the three cases. The distribution of ZnO dendrites is more homogeneous on SAM-modified ITO, and this is presumably attributed to the more homogeneous distribution of Pt NPs produced using the SAM method. Dendrites are more pronounced with infilled nanoparticles as observed from the SEM image by applying 267 mC/cm^2 (enlarged SEM images are provided in Fig. S17). As can be seen in Fig. 5b, 10% transmission was achieved for all samples in less than 30 s at a wavelength of 600 nm, which is much faster than the cases in Fig. 1 because of the higher metal ion concentration. Unlike the Zn electrodeposits produced with the lower concentration electrolyte, the charge densities at 10% transmission are all lower than the ideal thin film calculated by FDTD (dotted line) across all wavelengths (Fig. 5c). For example, Zn electrodeposits with Pt NPs SAM, spray-coated Pt NPs, and Pt NPs SAM with PVP experimentally yielded 23, 24, and 21 mC/cm^2 at 600 nm, respectively. In this case, there is a general trend in which the transmission decreases faster at shorter wavelengths, which is rationalized by the particle model structure described in Fig. 2. Transmission maps across the 400 to 1,000 nm wavelengths during 100 s of electrodeposition are shown in Fig. 5d ~ 5f.

For reference, similarly to the previous test with pristine ITO in the low concentration electrolyte, the spectroelectrochemical performance is also worse than any of the three cases above using the high concentration electrolyte with unmodified ITO (Fig. S3). The SEM images

indicate that there are differences in the growth pattern among the three cases, and that the electrodeposits consist of both nanoparticles and dendrites. Dendritic growth initially occurs, which is followed predominantly by nanoparticle growth that fills the space between dendrites. AFM confirms that the sizes of the pores in the surface are much smaller compared to the low-concentration electrolyte Zn electrodeposits in Fig. 1 (Fig. S18). The final thickness of electrodeposits by SEM shows that they are thicker than the thickness of ~127 nm for a uniform thin film of equivalent charge (Fig. S19), which implies the presence of a porous structure or oxidation-induced volume expansion. In the left side of the cross-sectional image in Fig. S19b, a porous structure is observed inside of a dendrite. Phase analysis with XRD also confirms that Zn and ZnO are both present in the electrodeposits (Fig. S6). With a practical two-electrode device, similar energy-efficient tinting is observed that is equivalent to the three-electrode configuration results (Fig. S20).

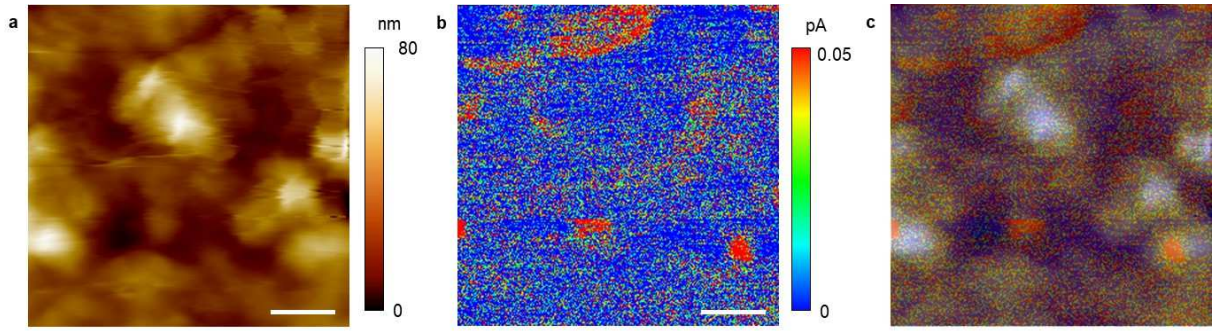

Fig. 6 Conductive atomic force microscopy of the dendritic region. (a) Surface height mapping. (b) Surface current mapping with 9 V external bias. (c) Overlapped image of (a) and (b). Scale bars are equal to 200 nm.

Surface current mapping by conductive AFM (C-AFM) is performed in the dendritic region of the Zn electrodeposits over ITO glass functionalized with spray-coated Pt NP after 30 s electrodeposition at −0.9 V vs. Zn/Zn^{2+}. As shown in Fig. 6a, the dendritic region is spatially distributed and partially aggregated by some regions of high heights of ~40 nm. The

corresponding current profile is given in Fig. 6b. Considering the overlapped height-current profiles in Fig. 6c, the regions of high heights tend to be more insulating than the background regions, which can be explained by assuming the dendrites consist of insulating ZnO. Therefore, dendritic regions of insulating ZnO will be used to build a model structure in FDTD simulations described in the next section. This coexistence of Zn and ZnO in Zn electrodeposits is also corroborated by XRD results (Fig. S6). An XRD spectrum of electrodeposits produced from the electrolyte that is sparged with N_2 and dried with molecular sieves produces a lower quantity of ZnO compared to the normal electrolyte (Fig. S21). This result suggests that some of the ZnO in the electrodeposits is produced during electrodeposition through reaction of the Zn with O_2 and/or H_2O.

2.5 Zn Dendrite Simulations

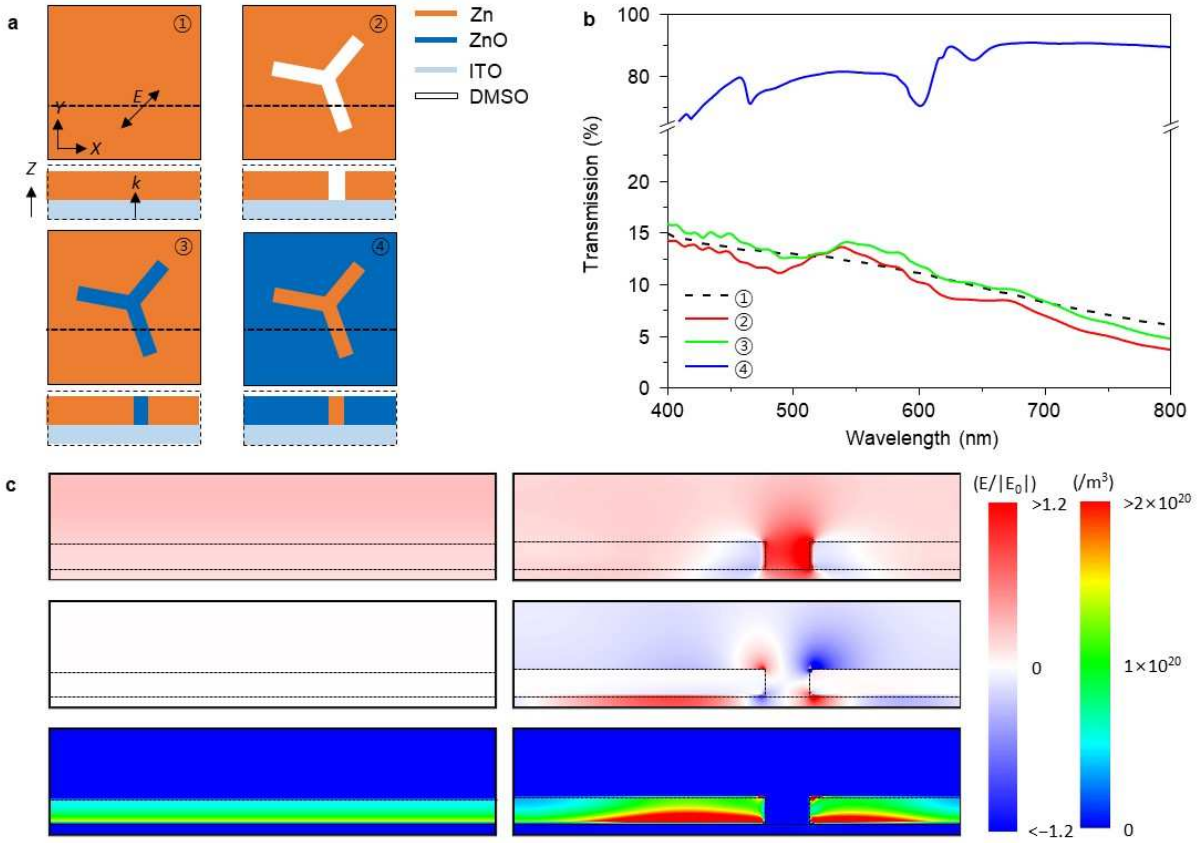

Fig. 7 Simulated transmission of dendritic structures. (a) Schematic of simulated structures with the same amount of charge density with respect to the 20 nm Zn thin film. 45-degree polarized plane-wave (electric field vector and wavevector are denoted as E and k) is illuminated from the ITO side to DMSO electrolyte. ① Zn thin film (20 nm). ② Zn film with cavity dendrite structure (22 nm). ③ Zn film with ZnO dendrite structure (21 nm). ④ ZnO film with Zn dendrite structure (30 nm). The dashed insets represent cross-sectional views. (b) Simulated transmission of the nanostructures in Fig. 7a. Cell size is fixed at 400 × 400 nm^2. (c) E_x field component mapping (top line), E_z field component mapping (middle line), and absorption mapping (bottom line). Left column is data from Case ①. Right column is data from Case ②. The cross-section is set to 90 × 400 nm^2 for 500 nm wavelength. Absorbed power per unit volume is normalized to the source power.

To understand the underlying optical phenomena of the dendritic Zn electrodeposits, a symmetrical radial pattern in which three rods are arranged at 120 degrees with respect to the center point was designed as a model dendritic structure (Fig. 7a). The height of the rods is modified according to the material assignment, but the size of one bar is equal to 40 nm × 150

nm. A 45-degree polarization which has polarization components in both the *X* and *Y* directions is adopted. The structures used in models ②~④ have equivalent charge densities as those of a 20 nm uniform thin film (①). Models are composed of a Zn thin film composed of hollow dendrites (②), a Zn thin film composed of ZnO-filled dendrites (③), and a ZnO thin film composed of Zn-filled dendrites (④). Transmissions of these model structures are displayed in Fig. 7b. In model ②, light blocking is improved compared to the thin film in most of the simulated spectral range. Another ideal situation (model ③), when this dendrite structure is all filled with compact ZnO, does not show pronounced light blocking except above around 700 nm. Considering the porosity of the experimental Zn electrodeposits, the actual structure can be interpreted as an intermediate result of ② and ③ (Fig. S22a). The inverse case of model ③ (model ④) has very poor light-blocking capabilities due to the large quantity of transparent ZnO in the structure, and its transmission profile does not match experimental observations. In addition, if too many dendrites exist, the transmission increases because the absorption from the metal itself decreases and the generated plasmons propagate readily (Fig. S22b). Rotation of the dendrites does not significantly affect the transmission (Fig. S23). Reversing the light propagation direction yields an equivalent result in Fig. 7b (Fig. S24). Reflection data show that the overall reflection is lowered in all models (②~④) compared to the perfectly uniform and compact Zn thin films (Fig. S25). Therefore, any decreases in transmission for models (②~③)

with respect to the thin film originate from increases in absorption. As the height of actual ZnO dendrite structure is slightly higher (<10%) than the background height, consideration of this condition to the simulation did not significantly change the transmission (Fig. S26).

This feature was investigated in more detail by looking at the electric field component and absorption profiles. By checking the cross-section at the dotted lines in Fig. 7 on models ① and ②, the E_x profile at a wavelength of 500 nm shows that the electric field is concentrated in the hole, unlike the thin film. In addition, the E_z component does not exist in the thin film and is identified only in the void dendrite model. The field profile is also similar at 700 nm (Fig. S27). This result shows that plasmon resonance occurs in the dendrite structure. The difference is more evident by comparing the absorption profiles (Figs. 7c and S27). More than twice the absorption is induced near the hole and along the Zn and ITO interfaces. With a ZnO filling, the absorption is less pronounced (Fig. S28). More light absorption compared to the thin film therefore results from enhanced absorption of light by the dendritic structure.

This model dendrite system can be understood as a set of well-known metal-dielectric-metal (MDM) slit structures. If the dielectric gap size (distance from metal to metal) is small, the surface plasmons, proximal to each metal wall, will behave like a single plasmon mode. In this case, the surface plasmon has a longer propagation length when more confined. If the size of this gap is appropriate, then plasmon modes generated on the metal wall can be hybridized with each other to form electrostatic (capacitive) modes without converging into one mode.[42, 43] The gap size that starts to form a hybridized surface plasmon is called the moderate gap size (w), which can be calculated as follows: $\frac{\lambda|\varepsilon_D|}{\pi|\varepsilon_M|}$, where λ is the wavelength of the incident light, ε_D and ε_M indicate the permittivities of the dielectric and metal, respectively, and π is a mathematical

constant. Usually, $|\varepsilon_D|$ and $|\varepsilon_M|$ decrease and increase, respectively, with increasing wavelength. Because *w* tends to decrease with increasing wavelength, a *w* at 500 nm wavelength is selected and considered for further discussions as a representative value. The *w* values of Zn-DMSO-Zn and Zn-ZnO-Zn structures are calculated to be 17 and 33 nm, respectively. As the simulated gap size (40 nm) is larger than the critical value *w* and smaller than the incident wavelength (subwavelength regime), hybridized surface plasmon modes exist with 500 nm incident light. In addition, the value of *w* at 700 nm incident light is 21 nm, which also meets the moderate gap condition. Increasing the size of the gap leads to an increase in plasmon propagation length, which increases transmission.[42-44]

There are three absorption mechanisms known in MDM slit structures, which are radiation, mirror, and metallic absorption loss.[45] Radiation loss occurs through re-emission of absorbed light toward the dielectric. Mirror loss is caused by tunneling that occurs when light approaches a Fabry-Perot cavity like the two-metal wall structure. Metallic absorption is another loss that is induced when light interacts with electrons inside the metal, which causes joule heating. Absorption in this slit structure is broadly distributed according to the size and shape of the slit. One strategy to enhance the absorption of the MDM slit is to increase the resonance inside the dielectric.[46] Increased transmission in model ③ can be comprehended from the reduced intensity of electric field between the Zn edges (Fig. S28). In terms of thickness, the transmission is expected to decrease exponentially when the slit height increases.[47, 48] A large quantity of dielectric in the structure obtained by inversing the structure composition (as in model ④) could increase transmission both by the intrinsic transmissive property of dielectrics

and by facilitating surface plasmon propagation from the metal wall into the dielectric medium.[49]

2.6 Electrodeposit Growth Modeling

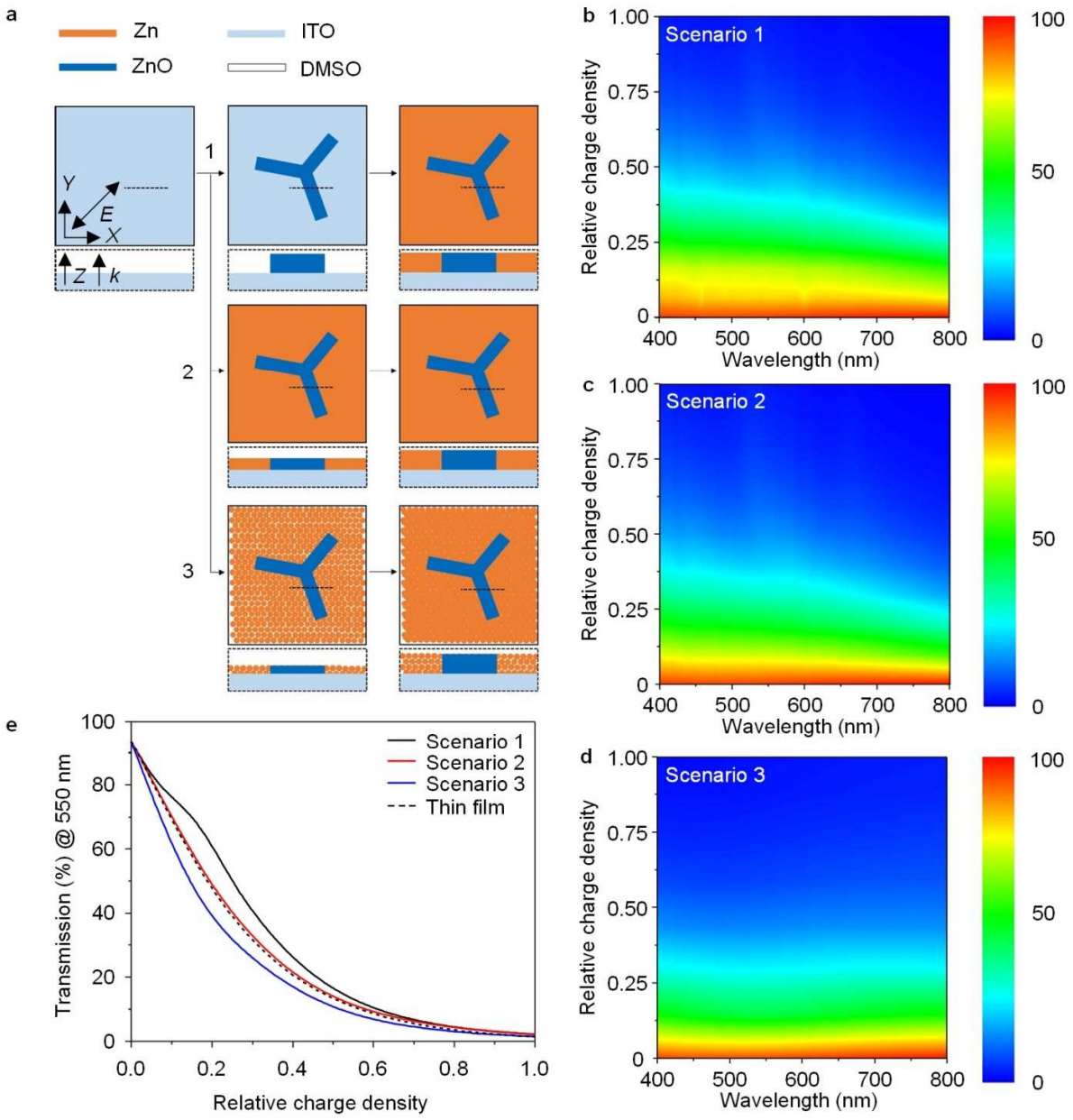

Fig. 8. Simulated transmission for different scenarios. 45-degree polarized plane wave (denoted as *E*) is illuminated from ITO side to DMSO. (a) Three growth models with charge density equivalent to a 40 nm Zn thin film. (b)-(d) Simulated transmission spectra with respect to the relative charge density (= (charge density equivalent to construct a structure) / (charge density of

40 nm thin film)). (b) corresponds to scenario 1. (c) corresponds to scenario 2. (d) corresponds to scenario 3 (close-packed hexagonal lattice with 10 nm radius sphere). (e) Comparison of transmission spectra at 550 nm between the three scenarios.

Although the exact in-situ growth morphological evolution for Zn electrodeposition is unknown, based on our above experimental findings and optical simulations, the optics of Zn electrodeposits during their growth were modeled according to three different scenarios. The three scenarios each have a final charge density (relative charge density = 1.0) equivalent to a 40 nm Zn thin film (Fig. 8a). In scenario 1, it is assumed that ZnO dendrites grow first, and subsequently the Zn thin film fills the area surrounding the ZnO dendrites. Scenario 2 assumes simultaneous growth of the ZnO dendrite and outside-filling of the Zn thin film at the same rate of thickness. Scenario 3 assumes simultaneous growth of the ZnO dendrites and formation of four layers of close-packed Zn nanoparticles at the same rate of thickness as depicted in the schema. As observed in Fig. 1 and Fig. 5, the experimentally observed transmission at shorter wavelengths decreases more rapidly. In scenarios 1 and 2 (Fig. 8b and 8c), on the contrary, transmission at longer wavelengths decreases more rapidly. Importantly, scenario 3 (Fig. 8d) follows the experimentally observed trend. These differences are clearer when comparing the transmission profiles at 550 nm (Fig. 8e). In contrast to experimental observation, scenario 1 possesses a transmission decrease rate that is slower than that of the thin film (Fig. 8e, dotted line). As seen in dendrite-based simulations (Fig. 7), the transmission profile of scenario 2 is quite similar to that of the thin film. However, in scenario 3, the transmission decreases much faster than in the ideal thin film, which matches our experimental observations. In all cases, increases in reflection are slower than that of the ideal thin film (Fig. S29). Taken together, these results demonstrate that the simultaneous growth of Zn nanoparticles and ZnO dendrites can fully explain the efficient light-blocking properties observed in reversible electrodeposition systems using Zn DMSO electrolytes.

2.7 Electrodeposits from Other Metals

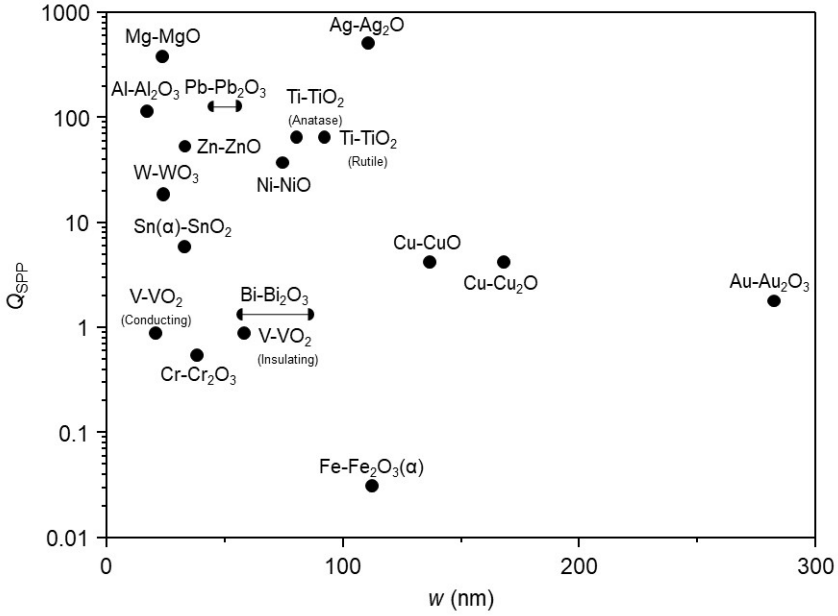

Fig. 9 Plot of moderate metal-dielectric-metal gap size (w) and surface plasmon quality factor for metal (Q_{SPP}) at 500 nm wavelength for various metal-metal oxide-metal gap systems.

Although the discussion thus far has focused exclusively on Zn-based nanostructures, we also investigated Ag as another metal-based system to evaluate the versatility and generality of the above results. Ag is a commonly used metal in reversible metal electrodeposition systems, and unlike Zn, it possesses pronounced plasmonic properties in the visible region. Considering the situations discussed above, charge density must be considered. The Zn 15 nm thin film has a charge of 32 mC/cm^2, while the Ag 15 nm thin film has a charge of 14 mC/cm^2. A 15-nm-thick Ag thin film has the same charge density as a 6.7-nm-thick Zn thin film. At the same thickness, Zn has more light-blocking properties, but when comparing films of the same charge density, Ag is more transparent at wavelengths less than around 600 nm compared to the Zn thin film (Fig. S30). Considering these points, the same simulation conditions in which the thin film is 15 nm as in Fig. 1 are used, but Zn is replaced with Ag. Calculation of the transmission gain yields, except for the case of $n = 1^2$, negative gain regardless of the direction of light below ~720 nm, and the

transmission approaches zero (Fig. S31). Even with a small amount of charge, these results suggest that Ag has the potential to have better light-blocking properties than Zn. By adopting the same structural components as in Fig. 5, dendrite simulations using Ag and Ag_2O also indicate better light-blocking property than a Zn-based system with many absorption peaks (Fig. S32).

The *w* values of Ag-DMSO-Ag and Ag-Ag_2O-Ag structures are 34 and 111 nm, respectively, at 500 nm. A large *w* value compared to the gap size indicates that the surface plasmons at both metallic walls do not form hybridized modes. The quality factor (Q_{SPP}) of surface plasmon polaritons is defined by $Q_{SPP} = \frac{(Re(\varepsilon_M))^2}{Im(\varepsilon_M)}$ and is the ratio of the real part and imaginary part of the permittivity.[50-52] It is a measure of plasmon resonance in the optical region of interest. Note that, the quality factor of localized surface plasmon resonances ($Q_{LSPR} = -\frac{Re(\varepsilon_M)}{Im(\varepsilon_M)}$) should be high when Q_{SPP} is high, and therefore Q_{SPP} also could be a measure of plasmon-induced absorption enhancement in nanoparticle arrays as discussed in Figs. 2 and 3. In Ag, Q_{SPP} is about 9.6 times higher than Zn at 500 nm. Therefore, the high absorption from Ag-based structures in simulation can be understood from the strong resonance of several surface plasmon modes. These effects would give rise to poor color neutrality in Ag films, which is undesired for most window applications. As shown in Fig. 9, although Au and Cu are well known for plasmonic applications in the visible spectrum, they would not be good choices in efficient light-blocking reversible metal electrodeposition systems due to their low Q_{SPP}. In contrast, Al- and Mg-based MDM dendritic structures should possess broad and strong absorption due to their low *w* and high Q_{SPP}, rendering these metal choices possibly better than Zn. While Al and Mg could be interesting candidates from an optical perspective, their low standard reduction potentials make designing reversible metal electrodeposition on transparent

conducting electrodes challenging. Detailed values of w and Q_{SPP} for various elements and corresponding references are summarized in Fig. S33. To check the validity of these analyses, we simulated a Cr-based dendrite void structure because the w of Cr-Cr_2O_3-Cr is less than the dendrite gap size (40 nm) like Zn, but its Q_{SPP} is ~97 times lower than Zn, so worse absorption than the thin film is expected. As shown in Fig. S34, the transmission simulations show that this expectation is met. For Cr, transmission is expected to increase with a dendritic void structure, which is the opposite of what was found for Zn.

Lastly, we consider potential differences in transmission caused by light propagation direction. $n = 1^2$ and 2^2 cases are adopted from the previous Zn and Ag particle simulations, which have equivalent charge density to the 15 nm thin film (Fig. S35). When $n = 2^2$, the transmissions are similar regardless of the direction and element, but when $n = 1^2$, it can be seen that there is a small difference depending on the direction, especially below about 600 nm. This phenomenon is called asymmetric transmission and occurs if scattering is dominant.[53, 54] If more scattering occurs within the films, a greater quantity of asymmetric transmission is expected.

3. Conclusions

In this work, we investigated Zn-based electrodeposits which could be potentially used in dynamic window technology due to their higher efficiency at blocking light compared to what is expected for an idealized uniform Zn thin film. Optical phenomena in the nanostructures are analyzed with FDTD methods. By modifying electrolyte conditions and Pt nanoparticle functionalization, we achieved two categories of Zn electrodeposits, nanoparticles with and without dendrites. Zn electrodeposits with dendrites exhibit lower than the theoretical charge density of uniform thin Zn films, which is advantageous for constructing high-contrast and large-

area dynamic windows. Close-packed Zn nanoparticles and dendrites with symmetrical radial patterns are modeled to analyze the optical phenomena underlying electrodeposit growth dynamics. In the nanoparticle model, absorption is enhanced due to hybrid surface plasmon resonance between the nanoparticles and the substrate. In the dendrite model, absorption is promoted near the Zn-dielectric-Zn gap from surface plasmon resonance in the metallic wall. We demonstrated the validity of the simulation by identifying an electrodeposit growth scenario consisting of simultaneous Zn nanoparticle growth and ZnO dendrite growth that matches surface characterization data (SEM and AFM) and the excellent light-blocking characteristics of the films. Lastly, we discussed how the optical understanding of these systems can be generalized to other metals such as Ag and Cr. Taken together, this in-depth level of understanding of the spectroelectrochemical properties of reversible metal electrodeposition could serve as a foundation for optical design principles in dynamic windows and other related applications.

4. Methods

4.1 Chemicals

Chemicals were received from commercial sources and used without further purification. Anhydrous DMSO was obtained from Millipore-Sigma. 3-mercaptopropionic acid (MPA) and $NaCH_3COO$ (99.99%) were obtained from Oakwood Chemical. $Zn(CH_3COO)_2$ (99.99%) was procured from ProChem, Inc. $ZnBr_2$ (99.999%) was purchased from Alfa Aesar. Hydroxyethylcellulose (average M_w ~ 90,000) and polyvinylpyrrolidone (PVP, average M_w ~ 55,000) were purchased from Sigma-Aldrich. The transparent conducting ITO glass substrates

(15 Ω/sq) were obtained from Xin Yan, Inc. An aqueous dispersion of Pt nanoparticles (3 nm in diameter, 1000 ppm) was procured from US Research Nanomaterials, Inc.

4.2 General Procedures

To prepare a low Zn concentration electrolyte, 50 mM $Zn(CH_3COO)_2$, 50 mM $ZnBr_2$, and 67 mM $NaCH_3COO$ were mixed together in DMSO. To prepare a high Zn concentration electrolyte, 300 mM $Zn(CH_3COO)_2$, 300 mM $ZnBr_2$, and 400 mM $NaCH_3COO$ were mixed together in DMSO and stirred for at least four hours. Hydroxyethylcellulose (2.0% w/v, average Mv ~ 90,000) is added to all electrolytes to form a gel and stirred for at least two hours. The concentration of PVP in the electrolytes was 1 μM in the PVP post-addition cases, and PVP is added after stirring of the hydroxyethylcellulose stirring is completed. MPA-functionalized ITO glass was achieved by dipping ITO glass electrodes in fresh ethanolic MPA solution (10 mM) for one day. Self-assembled Pt nanoparticles on ITO glass electrodes were prepared by dipping MPA-functionalized ITO glass on Pt nanoparticle dispersions diluted 1:10 with water for two days. Spray-coated Pt nanoparticle on ITO glass electrodes were prepared by spray-coating a 3:1 mixture of water:Pt nanoparticle dispersion. The Pt-modified ITO on glass substrates were then heated under air at 250°C for 20 min. For device fabrication, commercial Zn grids and butyl rubber (Solargain, Quanex, Inc.) were used.

4.3 Materials Characterization

Electrochemical tests were performed using a VSP-300 Biologic potentiostat in a 2 cm glass cube cuvette. −0.9 V vs. Zn/Zn^{2+} was applied in all chronoamperometry tests using separate Zn metal counter and reference electrodes, and an ITO on glass working electrode. Transmission measurements were conducted with a halogen light source and a spectrometer (Ocean Optics, Flame). Height AFM images were collected with a Nanosurf EasyScan 2 microscope operated in

contact mode using silicon tips coated with aluminum (ContAl-G, TedPella, Inc.). Conductive AFM images were collected with a NX-10 microscope operated with a conductive diamond coated tip (CDT-CONTR, Park Systems). Scanning electron microscope (SEM) images were obtained using a JOEL JSM-6010LA microscope with an operating voltage of 20 kV. X-ray diffraction (XRD) was conducted using a Bruker D2 X-ray Diffractometer.

4.4 Finite-difference time-domain (FDTD) simulation

Electromagnetic simulations were performed with a finite-difference time-domain (FDTD) program (Lumerical Solutions) to compute reflection, transmission, electric field distribution, and volume absorption profiles. Refractive indices of Zn, ZnO, Ag, Ag_2O, and ITO were taken from Werner et al.,[55] Adachi et al.,[56] Jiang et al.,[57] Xiao et al.,[58] and Konig et al.,[59] respectively. The refractive index of DMSO electrolyte was set constant as 1.4793.[60] A plane wave light source was imported over the simulation. Periodic boundary conditions were adopted for the *X*, *Y* dimension, and perfectly matched layer conditions were adopted for *Z* dimensions. 1 to 4 nm cubic meshes were used for structural modeling of the Zn nanostructure.

Acknowledgments

This research was supported by the Department of Energy's Office of Energy Efficiency and Renewable Energy (EERE) under the Building Energy Efficiency Frontiers in Innovation Technologies Program, Award Number DE-EE0009701, and the National Research Foundation of Korea funded by Korea government Ministry of Science and ICT (2021R1A2B5B03001851). We gratefully acknowledged the support of National Science Foundation (CHE1429768) for purchasing the X-ray diffractometer. SEM-EDX analysis was performed in the Mackay Microbeam Laboratory at UNR, and we thank Joel Desormeau and Luz Lim for their kind assistance.

CRediT authorship contribution statement

Cheon Woo Moon analyzed the data. **Cheon Woo Moon** and **Christopher J. Barile** wrote the paper. **Cheon Woo Moon**, **Nikhil C. Bhoumik, Profulla Mondol, Sung Hyuk Park, Ho Won Jang** performed the experiments. **Christopher J. Barile** conceived the project. All authors designed the experiments, discussed the results, and commented on the manuscript.

Data availability and Correspondence

Data that support the plots in this paper and other findings of this study are available from the corresponding author upon reasonable request. Correspondence to be made to Prof. Barile at cbarile@unr.edu

Declaration of Competing Interests

The authors declare that they have no known competing financial interests or personal relationships that could have appeared to influence the work reported in this paper.

References

[1] B.J. Van Ruijven, E. De Cian, I. Sue Wing, Nat. Commun. 10 (2019) 2762.

[2] R. Raslan, A. Ambrose, Nat. Energy, 7 (2022) 675-677.

[3] K. Allen, K. Connelly, P. Rutherford, Y. Wu, Energy Build. 139 (2017) 535-546.

[4] P.M. Congedo, C. Baglivo, A.K. Seyhan, R. Marchetti, J. Build. Eng. 42 (2021) 103057.

[5] M. Kim, D. Lee, S. Son, Y. Yang, H. Lee, J. Rho, Adv. Opt. Mater. 9 (2021) 2002226.

[6] D. Lee, M. Go, S. Son, M. Kim, T. Badloe, H. Lee, J.K. Kim, J. Rho, Nano Energy 79 (2021) 105426.

[7] B. Ko, J.-Y. Chae, T. Badloe, H. Kim, S.-J. Kim, S.-H. Hong, T. Paik, J. Rho, ACS Appl. Mater. Interfaces 14 (2022) 1404-1412.

[8] N. DeForest, A. Shehabi, J. O'Donnell, G. Garcia, J. Greenblatt, E.S. Lee, S. Selkowitz, D.J. Milliron, Build. Environ. 89 (2015) 107-117.

[9] A. Cannavale, U. Ayr, F. Fiorito, F. Martellotta, Energies 13 (2020) 1449.

[10] U.S. Department of Energy, Pathway to Zero Energy Windows: Advancing Technologies and Market Adoption, https://www.nrel.gov/docs/fy22osti/80171.pdf (2022) (accessed 24 May 2023).

[11] R. Baetens, B.P. Jelle, A. Gustavsen, Sol. Energy Mater. Sol. Cells 94 (2010) 87-105.

[12] A. Piccolo, F. Simone, J. Build. Eng. 3 (2015) 94-103.

[13] L. Luo, Y. Liang, Y. Feng, D. Mo, Y. Zhang, J. Chen, Crystals 12 (2022) 1426.

[14] V. Rai, R.S. Singh, D.J. Blackwood, D. Zhili, Adv. Eng. Mater. 22 (2020) 2000082.

[15] S.M. Islam, T.S. Hernandez, M.D. McGehee, C.J. Barile, Nat. Energy 4 (2019) 223-229.

[16] M.T. Strand, T.S. Hernandez, M.G. Danner, A.L. Yeang, N. Jarvey, C.J. Barile, M.D. McGehee, Nat. Energy 6 (2021) 546-554.

[17] O.S. Heavens, Optical properties of thin solid films, Courier Corporation1991.

[18] J. Xu, Y. Zhang, T.-T. Zhai, Z. Kuang, J. Li, Y. Wang, Z. Gao, Y.-Y. Song, X.-H. Xia, ACS Nano 12 (2018) 6895-6903.

[19] B. Yang, D. Ma, E. Zheng, J. Wang, Sol. Energy Mater. Sol. Cells 192 (2019) 1-7.

[20] S. Yan, L. Zhang, X. Lv, J. Sun, Y. Zhang, C. Zhang, Adv. Photonics Res. 3 (2022) 2000199.

[21] G. Wang, X. Chen, S. Liu, C. Wong, S. Chu, ACS Nano 10 (2016) 1788-1794.

[22] C.W. Moon, Y. Kim, J.K. Hyun, Nat. Commun. 13 (2022) 3391.

[23] Y. Li, T.F. Heinz, 2D Mater. 5 (2018) 025021.

[24] C.J. Barile, D.J. Slotcavage, J. Hou, M.T. Strand, T.S. Hernandez, M.D. McGehee, Joule 1 (2017) 133-145.

[25] J. Toudert, R. Serna, Opt. Mater. Express 7 (2017) 2299-2325.

[26] M. Sayed, J. Yu, G. Liu, M. Jaroniec, Chem. Rev. 122 (2022) 10484-10537.

[27] M.T. Strand, C.J. Barile, T.S. Hernandez, T.E. Dayrit, L. Bertoluzzi, D.J. Slotcavage, M.D. McGehee, ACS Energy Lett. 3 (2018) 2823-2828.

[28] D.C. Madu, S.M. Islam, H. Pan, C.J. Barile, J. Mater. Chem. C 9 (2021) 6297-6307.

[29] Q. Li, K. Du, K. Mao, X. Fang, D. Zhao, H. Ye, M. Qiu, Sci. Rep. 6 (2016) 29195.

[30] N. Hadilou, S. Souri, H. Navid, R. Sadighi Bonabi, A. Anvari, Sci. Rep. 12 (2022) 7829.

[31] R. Borah, R. Ninakanti, S. Bals, S.W. Verbruggen, Sci. Rep. 12 (2022) 15738.

[32] P.K. Jain, K.S. Lee, I.H. El-Sayed, M.A. El-Sayed, J. Phys. Chem. B 110 (2006) 7238-7248.

[33] E.G. Wrigglesworth, J.H. Johnston, Nanoscale Adv. 3 (2021) 3530-3536.

[34] V.G. Kravets, A.V. Kabashin, W.L. Barnes, A.N. Grigorenko, Chem. Rev. 118 (2018) 5912-5951.

[35] S.A. Maier, Plasmonics: fundamentals and applications, Springer (2007).

[36] Y. Huang, L. Ma, M. Hou, J. Li, Z. Xie, Z. Zhang, Sci. Rep. 6 (2016) 30011.

[37] J. Sanz, D. Ortiz, R. Alcaraz De La Osa, J. Saiz, F. González, A. Brown, M. Losurdo, H. Everitt, F. Moreno, J. Phys. Chem. C 117 (2013) 19606-19615.

[38] V. Devaraj, H. Jeong, C. Kim, J.-M. Lee, J.-W. Oh, Coatings 9 (2019) 387.

[39] Z. Fan, H. Men, Metals 12 (2022) 1454.

[40] J.-H. Han, M. Wang, P. Bai, F.R. Brushett, M.Z. Bazant, Sci. Rep. 6 (2016) 1-12.

[41] Y.-C. Ku, J.-W. Liaw, S.-Y. Mao, M.-K. Kuo, ACS Omega 7 (2022) 10420-10428.

[42] S. Collin, F. Pardo, J.-L. Pelouard, Opt. Express 15 (2007) 4310-4320.

[43] C.L. Smith, N. Stenger, A. Kristensen, N.A. Mortensen, S.I. Bozhevolnyi, Nanoscale 7 (2015) 9355-9386.

[44] R. Zia, M.D. Selker, P.B. Catrysse, M.L. Brongersma, J. Opt. Soc. Am. A 21 (2004) 2442-2446.

[45] K. Moon, T.-W. Lee, Y.J. Lee, S.-H. Kwon, Appl. Sci. 7 (2017) 86.

[46] C. Min, L. Yang, G. Veronis, Opt. Express 19 (2011) 26850-26858.

[47] C. Min, G. Veronis, Opt. Express 17 (2009) 10757-10766.

[48] J.S. White, G. Veronis, Z. Yu, E.S. Barnard, A. Chandran, S. Fan, M.L. Brongersma, Opt. Lett. 34 (2009) 686-688.

[49] A. Sellai, M. Elzain, Physica E: Low-Dimens. Syst. Nanostructures 41 (2008) 106-109.

[50] X. Fan, W. Zheng, D.J. Singh, Light: Sci. Appl. 3 (2014) e179-e179.

[51] D. Teng, Y. Tian, X. Hu, Z. Guan, W. Gao, P. Li, H. Fang, J. Yan, Z. Wang, K. Wang, Nanomaterials 12 (2022) 1950.

[52] P.R. West, S. Ishii, G.V. Naik, N.K. Emani, V.M. Shalaev, A. Boltasseva, Laser Photonics Rev. 4 (2010) 795-808.

[53] W. Brullot, T. Swusten, T. Verbiest, Adv. Mater. 27 (2015) 2485-2488.

[54] W. Liu, L. Huang, J. Ding, C. Xie, Y. Luo, W. Hong, Nanomaterials 11 (2021) 2410.

[55] W.S. Werner, K. Glantschnig, C. Ambrosch-Draxl, J. Phys. Chem. Ref. Data 38 (2009) 1013-1092.

[56] H.Y.H. Yoshikawa, S.A.S. Adachi, Jpn. J. Appl. Phys. 36 (1997) 6237.

[57] Y. Jiang, S. Pillai, M.A. Green, Sci. Rep. 6 (2016) 30605.

[58] X.-Y. Gao, H.-L. Feng, J.-M. Ma, Z.-Y. Zhang, J.-X. Lu, Y.-S. Chen, S.-E. Yang, J.-H. Gu, Phys. B: Condens. Matter 405 (2010) 1922-1926.

[59] T.A. Konig, P.A. Ledin, J. Kerszulis, M.A. Mahmoud, M.A. El-Sayed, J.R. Reynolds, V.V. Tsukruk, ACS Nano, 8 (2014) 6182-6192.

[60] X. Li, C. Wang, L. Ma, L. Liu, Infrared Phys. Technol. 125 (2022) 104313.

Vitae

Cheon Woo Moon has worked as a researcher at the University of Nevada, Reno, United States of America, in the Department of Chemistry since 2022. He obtained his Ph.D degree from the Seoul National University, Republic of Korea (2018). He worked as a researcher at the Ewha Womans University, Republic of Korea, from 2018 to 2022. His research focuses on active plasmonic materials towards solar-to-fuel conversion, smart windows, imaging and displays, sensors, and batteries.

Nikhil Chandra Bhoumik is a researcher in the field of electrochemistry. He obtained his Master's and M.Phil. Degrees in Inorganic Chemistry from Jahangirnagar University, Bangladesh. In 2021, he embarked on his Ph.D. studies in the Department of Chemistry at the University of Nevada, Reno, USA. His research encompasses the development of dynamic windows using reversible metal electrodeposition, metal-ion batteries, and organometallic chemistry.

Profulla Mondol has been a Ph.D student in the Department of Chemistry, University of Nevada, Reno, USA, since 2019. He earned his BS and MS degrees in Chemistry from Jahangirnagar University, Savar, Dhaka, Bangladesh in 2016 and 2018, respectively. In his Ph.D, he is working on the development of non-precious metal electrocatalysts for oxygen reduction reaction and nitrate reduction reaction under the supervision of Prof. Christopher Barile.

Sung Hyuk Park is currently a Ph.D. candidate under the supervision of Prof. Ho Won Jang in the Department of Materials Science and Engineering of Seoul National University (SNU). He received his BS degree in Material Science and Engineering from Yonsei University, Seoul, Korea, in 2021. His current research focuses on the physics of hafnia-based ferroelectrics, the ferroelectric tunnel junctions of non-volatile memory devices and epitaxial growth of oxides.

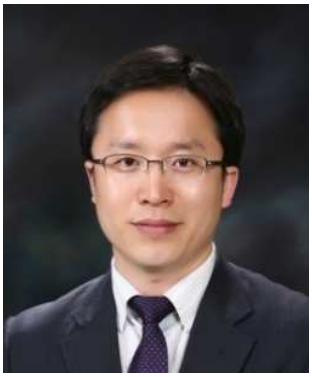

Ho Won Jang is a professor of the Department of Materials Science and Engineering in Seoul National University. He earned his Ph.D. from the Department of Materials Science and engineering in Pohang University of Science and Technology in 2004. He worked as a research associate at the University of Madison-Wisconsin from 2006 to 2009. Before he joined Seoul National University in 2012, he worked in Korea Institute of Science and Technology (KIST) as a senior research scientist. His research interests include materials synthesis and device

fabrication for ferroelectrics, memristors, solar water splitting cells, chemical sensors, plasmonics, and metal-insulator transition.

Christopher J. Barile is the Clemons-Magee Professor in the chemistry department at the University of Nevada, Reno. Prof. Barile earned BSc. with distinction and co-terminal MSc. degrees in chemistry from Stanford University. He then attended the University of Illinois at Urbana-Champaign and earned his PhD focusing on the development of next-generation battery technologies. Prof. Barile subsequently returned to Stanford as a postdoctoral scholar in materials science and engineering before launching his independent career in 2017. His research lies at the intersection of electrochemistry, inorganic chemistry, and materials chemistry with an emphasis on solving problems associated with energy conversion, storage, and efficiency.

Graphical abstract

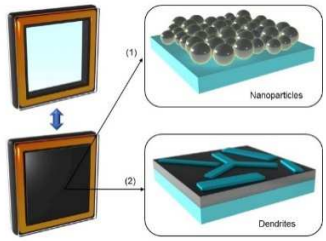

Plasmon resonance in nanoparticle and dendritic nanostructures enables dynamic windows based on reversible Zn electrodeposition to switch with exceptionally low charge density.

Highlights

• Zn nanostructures lead to lower charge density than that of an ideal perfectly uniform Zn thin film.

• Plasmon resonance of Zn electrodeposits arises from synergy between Zn nanoparticles and ZnO dendrites.

• A design principle for high-contrast reversible metal electrodeposition-based smart window is proposed.